remote sensing

MDPI

Article

Monitoring Bedfast Ice and Ice Phenology in Lakes of the Lena River Delta Using TerraSAR-X Backscatter and Coherence Time Series

Sofia Antonova [1,*], Claude R. Duguay [2], Andreas Kääb [3], Birgit Heim [1], Moritz Langer [4], Sebastian Westermann [3] and Julia Boike [1]

1 Alfred Wegener Institute, Helmholtz Center for Polar and Marine Research, Potsdam 14473, Germany; birgit.heim@awi.de (B.H.); julia.boike@awi.de (J.B.)
2 Department of Geography & Environmental Management and Interdisciplinary Centre on Climate Change, University of Waterloo, Waterloo, ON N2L 3G1, Canada; crduguay@uwaterloo.ca
3 Department of Geosciences, University of Oslo, Oslo 0316, Norway; a.m.kaab@geo.uio.no (A.K.); sebastian.westermann@geo.uio.no (S.W.)
4 Department of Geography, Humboldt-Universität zu Berlin, Berlin 10099, Germany; moritz.langer@geo.hu-berlin.de
* Correspondence: sofia.antonova@awi.de; Tel.: +49-331-288-2200

Academic Editors: Deepak R. Mishra, Xiaofeng Li and Prasad S. Thenkabail
Received: 12 September 2016; Accepted: 24 October 2016; Published: 3 November 2016

Abstract: Thermokarst lakes and ponds are major elements of permafrost landscapes, occupying up to 40% of the land area in some Arctic regions. Shallow lakes freeze to the bed, thus preventing permafrost thaw underneath them and limiting the length of the period with greenhouse gas production in the unfrozen lake sediments. Radar remote sensing permits to distinguish lakes with bedfast ice due to the difference in backscatter intensities from bedfast and floating ice. This study investigates the potential of a unique time series of three-year repeat-pass TerraSAR-X (TSX) imagery with high temporal (11 days) and spatial (10 m) resolution for monitoring bedfast ice as well as ice phenology of lakes in the zone of continuous permafrost in the Lena River Delta, Siberia. TSX backscatter intensity is shown to be an excellent tool for monitoring floating versus bedfast lake ice as well as ice phenology. TSX-derived timing of ice grounding and the ice growth model CLIMo are used to retrieve the ice thicknesses of the bedfast ice at points where in situ ice thickness measurements were available. Comparison shows good agreement in the year of field measurements. Additionally, for the first time, an 11-day sequential interferometric coherence time series is analyzed as a supplementary approach for the bedfast ice monitoring. The coherence time series detects most of the ice grounding as well as spring snow/ice melt onset. Overall, the results show the great value of TSX time series for monitoring Arctic lake ice and provide a basis for various applications: for instance, derivation of shallow lakes bathymetry, evaluation of winter water resources and locating fish winter habitat as well as estimation of taliks extent in permafrost.

Keywords: lake ice; bedfast ice; ice phenology; SAR; TerraSAR-X; backscatter intensity; interferometric coherence; time series; Lena River Delta; CLIMo

1. Introduction

Thermokarst lakes and ponds are abundant and characteristic landscape features of the Arctic lowland permafrost regions on both the Eurasian and North American continents. Estimates of their areal coverage span a wide range and are scale dependent [1–3], but all agree that they can occupy a significant proportion of the land area in high latitude regions (up to 40% in some areas [3]). Arctic water bodies play a crucial role in land-atmosphere exchanges of greenhouses gases and energy

fluxes [4–7], making them highly important for global climate change science. The seasonal ice cover can reach thicknesses of up to 2 m over an ice season of up to 8–9 months which alters greenhouse gas fluxes, as well as biological productivity within these water bodies. The ice-cover duration is also an important indicator of climate variability and knowledge of lake ice phenology from freeze onset to water-clear-of-ice is important in particular for regional climate change assessments [8,9].

Shallow water bodies which have depths of less than the maximum ice thickness eventually experience grounding to the bottom (i.e., bedfast ice) during the winter time. After ice grounding, such water bodies significantly decrease their contribution to energy and gas fluxes as the biological activity is suppressed within the frozen sediments [10,11]. Deeper water bodies where unfrozen water remains beneath the ice cover during the entire winter period favor the development of a talik (permanently unfrozen inclusion within permafrost). Therefore, distinguishing grounded from floating ice areas in high latitude lakes is essential for permafrost science from physical, chemical and biological aspects. Changes in lake ice regime from a floating to a grounded state and vice versa, due to water level change or ice thickness variations, can also be used as an indicator of climate variability [12,13]. Variations in the fraction of ice that freezes to bed can also be a result of lake drainage or lake expansion indicating landscape transformations caused by local impacts of climate change [14].

Monitoring lake ice phenology and the fraction of bedfast ice using ground observations is not possible on a regular basis and over larger areas in remote Arctic territories. Remote sensing can provide frequent and spatially representative information on the ice regime of Arctic lakes. Optical remote sensing in the Arctic is limited due to polar night and often persistent cloud cover [15,16]. Active microwave radar signals, on the other hand, penetrate through cloud cover and allow for systematic monitoring of lake ice phenology [17–20]. Moreover, the difference in radar backscatter intensities between grounded (bedfast) and floating lake ice allows for mapping of these areas and estimation of the timing of grounding. The application of radar technology for this purpose began in the 1970s when airborne radar systems were used to acquire images over Alaskan lakes [21–23]. These early studies were limited to the visual (qualitative) interpretation of imagery since no calibrated digital data were available. In the new era of spaceborne Synthetic Aperture Radar (SAR) in the 1990s, a number of studies utilized calibrated ERS-1 data (C-band) and the quantitative analysis of backscatter intensity for different periods during ice growth [24–26]. However, the relatively low spatial resolution of SAR data used in these studies (240 m pixel size) confined the analysis to relatively large lakes, omitting the abundant number of water bodies smaller than the resolution. Advancements in technology have allowed for lake ice studies using higher spatial resolution (100 m or better) data from C-band RADARSAT-1, ERS-1 and ENVISAT ASAR [12,13,27–29]. One of the main constraints for SAR-based investigations to date has been the insufficient temporal resolution of time series, so that acquisitions obtained with different incidence angles or a multi-sensor approach must be employed [20,27]. Monitoring lake ice conditions using X-band SAR data has mostly been limited to the early airborne studies mentioned above. The potential of data from new generation X-band SAR, such as TSX with its spatial resolution up to 3 m, is far from fully investigated. Using a single high-resolution Spotlight TSX image, Jones et al. [30] showed its excellent suitability for distinguishing bedfast from floating lake ice. Sobiech and Dirking [31] used TSX imagery for the classification of ice and open water fractions during the ice decay period in lakes of the Lena River Delta. To our best knowledge, the latter study is also the only example of SAR-based investigation of lake ice conditions in the Siberian Arctic.

SAR-derived timing of ice grounding in combination with bathymetry information can be used as a proxy for the estimation of ice growth [28,29]. Another approach is to use a numerical ice growth model: SAR-derived date of ice grounding can be assigned to a simulated ice thickness on that date, which, in turn, provides information on the depth of a lake (i.e., bathymetry) [26,32].

In this study, we investigate the potential of high temporal resolution (11-day) TSX backscatter intensity time series for monitoring ice phenology and ice grounding during three years on lakes in the Lena River Delta, Siberia. In addition, for the first time, we produce a sequential interferometric

coherence time series for detection of ice grounding and compare it to the backscatter intensity time series. Using TSX-derived timing of ice grounding and the numerical lake ice model CLIMo, we retrieve the thickness of bedfast ice and evaluate the results against in situ measured ice thicknesses.

2. Background on SAR Response to Lake Ice

2.1. Ice Grounding

Interactions between radar and ice cover are strongly dependent on backscattering interfaces [33]. In the case of floating ice, there is a strong dielectric contrast between ice and the water beneath: the real component of the relative dielectric permittivity of fresh water at 0 °C for X-band frequencies is ~43 [34] and that of freshwater ice is ~3 [35]. This large dielectric contrast causes a strong reflectance of the radar signal from the ice–water interface. Using polarimetric analysis, recent studies have demonstrated that the single bounce at this interface is the main mechanism of backscattering from the floating ice [36,37]. Thus, backscatter intensity in the case of floating ice is mostly controlled by roughness at the ice–water interface. In the case of grounded ice, there is no sharp dielectric contrast between the ice and the frozen sediments as the relative permittivity for frozen silt and clay is ~3–6 [38]. Absence of the dielectric contrast leads to a strong signal absorption into the frozen sediments causing much lower backscatter intensity compared to floating ice. Thus, the rapid decrease of backscatter intensity during wintertime can indicate the change from floating ice to grounded ice conditions. Various studies have documented the magnitude of the drop in backscatter intensity with ice grounding at different radar frequencies (Table 1). The variations in the magnitude of backscatter drop between different studies are likely associated with sensor settings (frequency, incidence angle, polarization) as well as regional settings (composition and structure of lake sediments, frozen/unfrozen condition of sediments or wetness of sediments).

Table 1. Magnitude of the drop in backscatter intensity with ice grounding documented in different studies.

Reference	Study Area	Sensor	Polarization	Incidence Angle	Magnitude of Drop in Backscatter from Floating to Grounded Ice (in dB)
Jeffries et al. [24]	Alaska North Slope	ERS-1 (C-band)	VV	20.1–25.9°	10–12
Morris et al. [25]	Alaska North Slope, Yukon Delta, Bristol Bay	ERS-1 (C-band)	VV	20.1–25.9°	4.8–8.8 (sub-Arctic lakes) 7.8–11.8 (Arctic lakes)
Duguay et al. [27]	Churchill, Manitoba	RADARSAT-1 (C-band)	HH	20–49°	6
Brown et al. [39]	Sagavanirktok River delta, Alaska	ASAR AP (C-band)	HH, VV HV, VH	19.2–31.4°	threshold: −10 * threshold: −19
Engram et al. [36]	northern Seward Peninsula, Arctic Coastal Plain	ALOS PALSAR, JERS-1 (L-band) ERS-1,-2 (C-band)	HH VV	24–40° 23°	3–6 8–9
Jones et al. [30]	Arctic Coastal Plain	TSX (X-band)	HH	46°	threshold: −12.3
Gunn et al. [40]	Churchill, Manitoba	Field-based scatterometer (X- & Ku-band)	VV, VH	39–45°	2–4

* In case a time series was not present in the study, a fixed threshold value set to differentiate floating from grounded ice is indicated.

Repeat-pass SAR interferometry (InSAR) employs the phase of the radar signal to detect surface displacements. It calculates the phase difference between two SAR images covering the same area at different times. Usage of InSAR can be strongly limited due to insufficient phase coherence between two SAR images. Potential reasons for a loss of phase coherence include thermal noise from the antenna, a large interferometric baseline, topographic effects, misregistration between the SAR images, atmospheric effects, as well as surface changes that occur between SAR acquisitions [41]. In case of lake ice, such surface change is defined by the continuously evolving ice–water interface, with ice

growth changing the backscattering interface at each SAR acquisition. Therefore, for floating ice the coherence is expected to be constantly low because the ice–water interface is never the same over the entire winter period. However, once the ice becomes grounded, the backscattering interface does not change significantly (depending largely on the freezing front expanding into the sediments), causing potentially an increase in coherence. Thus, we expect an increase in coherence to be a good indicator of ice grounding, in addition to the decrease in backscatter.

2.2. Ice Phenology

Monitoring ice phenology using SAR backscatter is possible by associating backscatter variations to changes in the backscattering potential of the ice medium. Initial freeze-up (or ice-on) is characterized by low backscatter due to specular reflection from a thin and smooth undeveloped ice cover. At the beginning of ice formation, C-band backscatter intensity values for thin, smooth ice have been reported to range from −22 to −16 dB (ERS-1, VV) [24], −16 to −13 dB (RADARSAT-1, HH) [27] and −15.9 dB to −4.8 dB (ASAR, HH) and −17.4 dB to −11.7 dB (RADARSAT-2, HH) [20]. However, it can be difficult to detect initial ice formation due to similarly low backscatter of newly formed ice and open water under calm wind conditions. The potential presence of cracks and ridges in the ice, which appear as bright linear features contrasting against the surrounding dark lake surface, can support the detection of early freeze-up [25]. Ancillary data, such as air temperature observations from nearby meteorological stations, can also help with freeze-up detection.

Ice growth (thickening) is marked by an increase in backscatter up to a saturation point after which the backscatter remains relatively stable until melt onset (if the ice has not grounded). We designate this period of stable backscatter as a "stable stage". Jeffries et al. [24] and Morris et al. [25] report backscatter values between −6 dB and −7 dB (ERS-1 VV, 20.1°–25.9° incidence angle) and Duguay et al. [27] report values from −9 to 2 dB (RADARSAT-1, HH, 20°–27° incidence angle) for floating ice during the stable stage. Howell et al. [18] state a difference of 6 dB between the stable stage and freeze onset for QuikSCAT (Ku-band, HH, 46° incidence angle) time series of Great Bear and Great Slave lakes (Canada). Threshold values of the same order of magnitude are given in [20] for ASAR (HH, 15°–42° incidence angle) (5.5 dB) and RADARSAT-2 (HH, 20°–46° incidence angle) (6.5 dB) time series.

Melt onset is characterized by a significant alteration of backscatter intensity compared to the stable stage. Generally, melt onset begins with snow melt on the top of the ice cover (if snow is present). Therefore, backscatter variations during melt onset depend mainly on snow cover properties. Wet snow typically causes high absorption of a SAR signal and consequently a significantly reduced backscatter intensity. Additionally, water ponding on the ice surface can reduce backscatter intensity due to specular reflection of the radar signal away from the ponding surface. However, when the snow cover melts and refreezes due to day and night air temperature variations around 0 °C, the backscatter intensity can increase due to increased roughness on the snow cover surface. Jeffries et al. [24] observe both ERS-1 backscatter decrease and increase of 10 dB for different locations during the melt period. Duguay et al. [27] report RADARSAT-1 backscatter intensity as low as −21 to −12 dB for the melt period. Howell et al. [18] observe a pronounced decrease in Ku-band backscatter with melt onset and found a difference of 4 dB between the stable stage and melt onset. Geldsetzer et al. [42] report RADARSAT-2 (HH) backscatter values of about −21 dB from lake ice following melt onset. Surdu et al. [20] indicate backscatter values ranging from −20.4 to −15.7 dB (ASAR) and from −22.9 to −16.1 dB (RADARSAT-2) at the beginning of break up period.

Water clear of ice (or ice-off), which corresponds to the date when the water body becomes totally ice free at the end of break-up period, can be easily identified by low backscatter values under calm wind conditions due to specular reflection of the radar signal away from the water surface. However, under windy conditions, the roughened water surface causes high backscatter, so that the detection of water clear of ice becomes difficult. Howell et al. [18] observe a difference of 10 dB between the stable stage and water clear of ice from QuikSCAT Ku-band scatterometer time series, while Surdu et al. [20] report a difference of 7.5 dB for ASAR and 8.5 dB for RADARSAT-2.

3. Study Area

The Lena River Delta (73°N, 126°E) in Siberia occupies an area of about 30,000 km^2 and is located in the zone of continuous permafrost that reaches depths of up to 600 m [43]. The region belongs to the typical Arctic tundra ecozone. Water bodies of different size cover about 20% of the delta's land area [44]. The climate of the Lena River Delta area is characterized by extremely cold, long winters and short, cool summers. Boike et al. [45] described the recent climatic characteristics of the region based on regular measurements on Samoylov Island in the southern part of the delta (Figure 1) during the period from 1998 to 2011. The annual mean air temperature was −12.5 °C with February mean temperatures of −33.1 °C and July mean temperatures of 10.1 °C. Rainfall usually took more than half of annual precipitation with a mean of 125 mm. Snow accumulation usually began in October and snow melt typically started in the second half of May and lasted until early June. The snow depth featured high spatial heterogeneity due to microtopographic features (i.e., polygonal relief) and snow redistribution by wind, but typically did not exceed several decimeters.

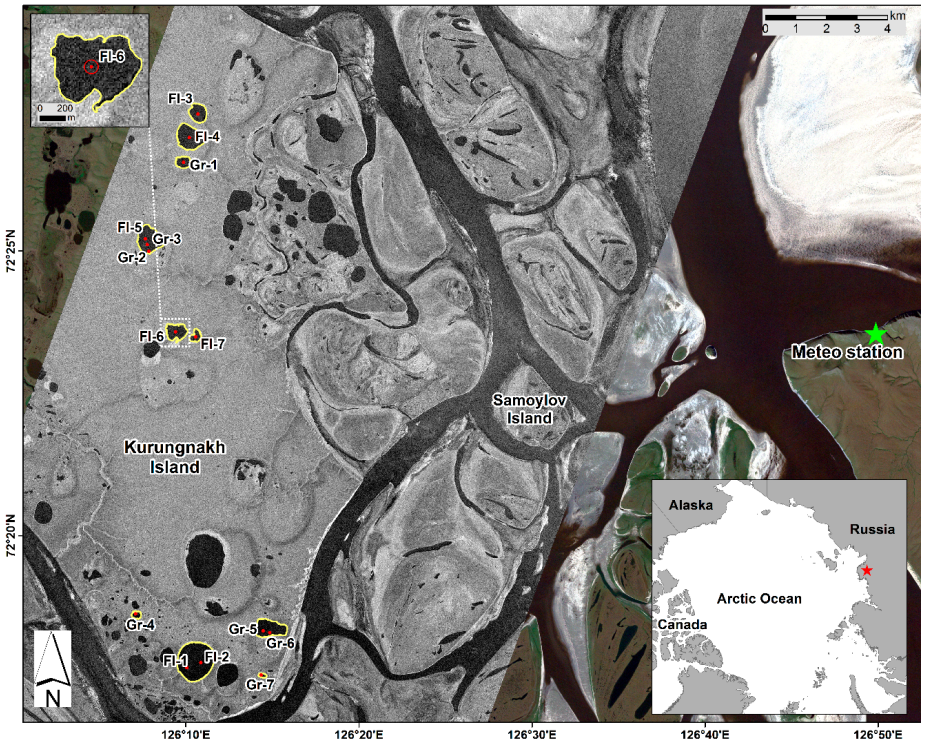

Figure 1. TSX backscatter intensity image from 25 August 2012 (underlain by a RapidEye image; RGB 3-2-1) of the study area with lakes of this study delineated in yellow. Drilling locations in April 2015 are marked as red dots. The meteorological station is marked as a green star. The upper left inset shows an example of a region of interest (ROI) around the drilling location. In the lower right inset, the location of the study area is marked as a red star.

In this study, we focus on the southern part of the delta, particularly on Kurungnakh-Sise (or Kurungnakh) Island (Figure 1). The main part of the island consists of Pleistocene Ice Complex deposits (also known as Yedoma), which are underlain by fluvial sands and covered by a thin Holocene layer. The island has a maximum elevation of 55 m a.s.l. On its generally flat surface, deep thermokarst lakes and basins have made incisions as a result of permafrost degradation that started about 12 ka ago. About 7.5% and 38% of the island area is covered by thermokarst lakes and basins, respectively. Only 16% of the total basin area is occupied by remaining lakes, indicating past and current drainage processes [46].

4. Data and Methods

4.1. In Situ Measurements

In order to evaluate the potential of TSX to monitor ice grounding, in situ ice thickness measurements were collected at 14 locations from a sample of 10 lakes in April 2015 (Figure 1, Table 2). Additionally, snow depth on the ice surface and water depth beneath the ice cover (if present) were measured. Seven of these locations featured grounded ice and the other seven floating ice. In the following, we refer to the former locations as "shallow" and the latter as "deep".

Table 2. Coordinates of measurements and measured parameters in April 2015. Grey shading is for the shallow locations where the ice was determined to be grounded. Total depth in the last column includes ice thickness and water depth beneath (if present).

No.	Date	Name	Lon, E	Lat, N	Snow Cover, m	Ice Thickness, m	Total Depth, m
1	13 April 2015	Fl-1	126.1785	72.2987	0	1.90	4.55
2	13 April 2015	Fl-2	126.1653	72.2971	0	1.98	6.45
3	20 April 2015	Fl-3	126.1507	72.4592	0.28	1.55	5.00
4	20 April 2015	Fl-4	126.1433	72.4522	0.15	1.65	2.40
5	20 April 2015	Gr-1	126.1390	72.4449	0.15	1.80	1.80
6	20 April 2015	Fl-5	126.1052	72.4220	0.15	1.65	2.35
7	20 April 2015	Gr-2	126.1092	72.4184	0.18	1.60	1.60
8	20 April 2015	Gr-3	126.1074	72.4203	0	1.54	1.54
9	20 April 2015	Fl-6	126.1389	72.3952	0.24	1.65	2.55
10	20 April 2015	Fl-7	126.1586	72.3940	0.42	1.70	2.50
11	20 April 2015	Gr-4	126.1134	72.3121	0	1.58	1.58
12	20 April 2015	Gr-5	126.2370	72.3088	0	1.05	1.05
13	20 April 2015	Gr-6	126.2436	72.3084	0	1.10	1.10
14	13 April 2015	Gr-7	126.2371	72.2959	0	1.70	1.70

4.2. SAR Data

TSX is a synthetic aperture radar (SAR) satellite, operating at X-band (wavelength 3.1 cm, frequency 9.6 GHz). The SAR time series used in this study includes 95 StripMap Single-Look Slant Range Complex (SSC) images acquired by TSX between August 2012 and October 2015, at approximately 08:34 local time (22:34 UTC). The time span between acquisitions was 11 days, with a few exceptions when the time spans were 22 and 44 days. The slant range and azimuth pixel spacing is 0.9 m and 2.4 m, respectively. The scene covered an area of approximately 18 km $\times$ 56 km. The chosen orbit was in descending overpass and the radar was right-looking. The acquisition incidence angles were between 31.6° and 31.7°, and polarization was HH for all images.

4.3. SAR Data Processing

The data were processed using the commercial radar software Gamma [47]. SSC data were converted to Gamma Single Look Complex (SLC) format and the SLC data were then consecutively co-registered with a subpixel accuracy (typically better than 0.2 pixel). The co-registered SLC data were multi-looked by factors of 4 and 3 in range and azimuth directions, respectively, in order to obtain intensity values with reduced speckle and roughly square ground range pixels. Intensity images were calibrated to sigma naught and converted to dB using:

$$\sigma^0_{dB} = 10\lg(k_s \times |DN|^2 \times sin\theta), \quad (1)$$

where k_s is the calibration constant, DN is the amplitude of a complex number representing a pixel value of SLC data, and θ is the local incidence angle.

Interferometric coherence is the magnitude of the complex cross-correlation coefficient of an SAR image pair. The cross-correlation coefficient was computed using:

$$\rho(x,y) = \frac{\langle s_1(x,y)\, s_2^*(x,y)\rangle}{\sqrt{\langle |s_1|^2\rangle \langle |s_2|^2\rangle}}, \quad (2)$$

where ρ is the coherence value at pixel location (x,y), s_1 and s_2 are the complex values of SLC images 1 and 2 at pixel location (x,y), and * stands for the complex conjugation. The spatial averaging (marked by $\langle\rangle$) was processed over a window of 3 × 3 pixels. 83 coherence images, each with a temporal baseline of 11 days, were obtained from interferometric pairs of SLC images.

Both the backscatter intensity images and the coherence images were geocoded to the WGS84 ellipsoid with a pixel size of 10 m × 10 m in the Universal Transverse Mercator (UTM) projection Zone 52N. A region of interest (ROI) was created around each in situ ice thickness measurement location as a circle with a diameter of approximately 10 pixels (Figure 1). Mean backscatter intensity and coherence values were extracted for each ROI of the images analyzed.

4.4. Lake Ice Model

The one-dimensional thermodynamic Canadian Lake Ice Model CLIMo [48] was used to simulate ice thickness and ice dates (ice-on and ice-off). We used the simulated ice thickness to retrieve depth of the shallow locations based on TSX backscatter intensity changes. One of the advantages of the model is that it takes into account overlying snow cover, which is a key factor for ice growth. CLIMo is described in detail in [48] and has previously been shown to perform very well for the estimation of ice thickness of shallow Arctic water bodies [13,33,48–50].

In this study, the model was forced for two lake depths representing the minimum and maximum depths of the lakes sampled in the field (1.05 m and 6.45 m; Table 2) using daily mean meteorological data obtained from a station located approximately 20 km to the east of the area of investigation (Figure 1). Input data include air temperature, relative humidity, wind speed, cloud cover and snowfall [51]. No snow density measurements were collected in the field in 2015 and past snow density from the area was measured only for land [45]. Sturm and Liston [52] reported about 20% higher density for lake snow than for land snow on the Arctic Coastal Plain, Alaska and provided average lake snow density value of 330–340 kg/m^3. We used a constant dry snow density value of 330 kg/m^3 in our model simulations. Besides ice thickness, the model output provides snow depth calculated from the input snowfall. Wind driven snow redistribution across the lakes is common on Arctic lakes and in our study area (see Table 2). Therefore, model simulations were performed using different snow cover scenarios from 0% to 100% of the precipitation-derived snow depth, with 0 corresponding to a snow free lake ice surface and 100% to the full amount of the calculated snow depth. In situ snow depth measurements on the lakes (Table 2) showed a wide range, corresponding to model scenarios from 0% to >200% of the snow cover. However, these measurements represented snow depth at specific points on a particular date (13 or 20 April 2015). Therefore, they did not necessarily capture the actual snow depth across the lakes, but rather exemplify the snow depth variability and possible ranges.

5. Results

Figure 2 shows time series of TSX backscatter for the deep and shallow lake locations as well as air temperatures for the period from August 2013 to October 2015. These times series are used for the bedfast ice detection and monitoring, as well as for the interpretation of ice phenology.

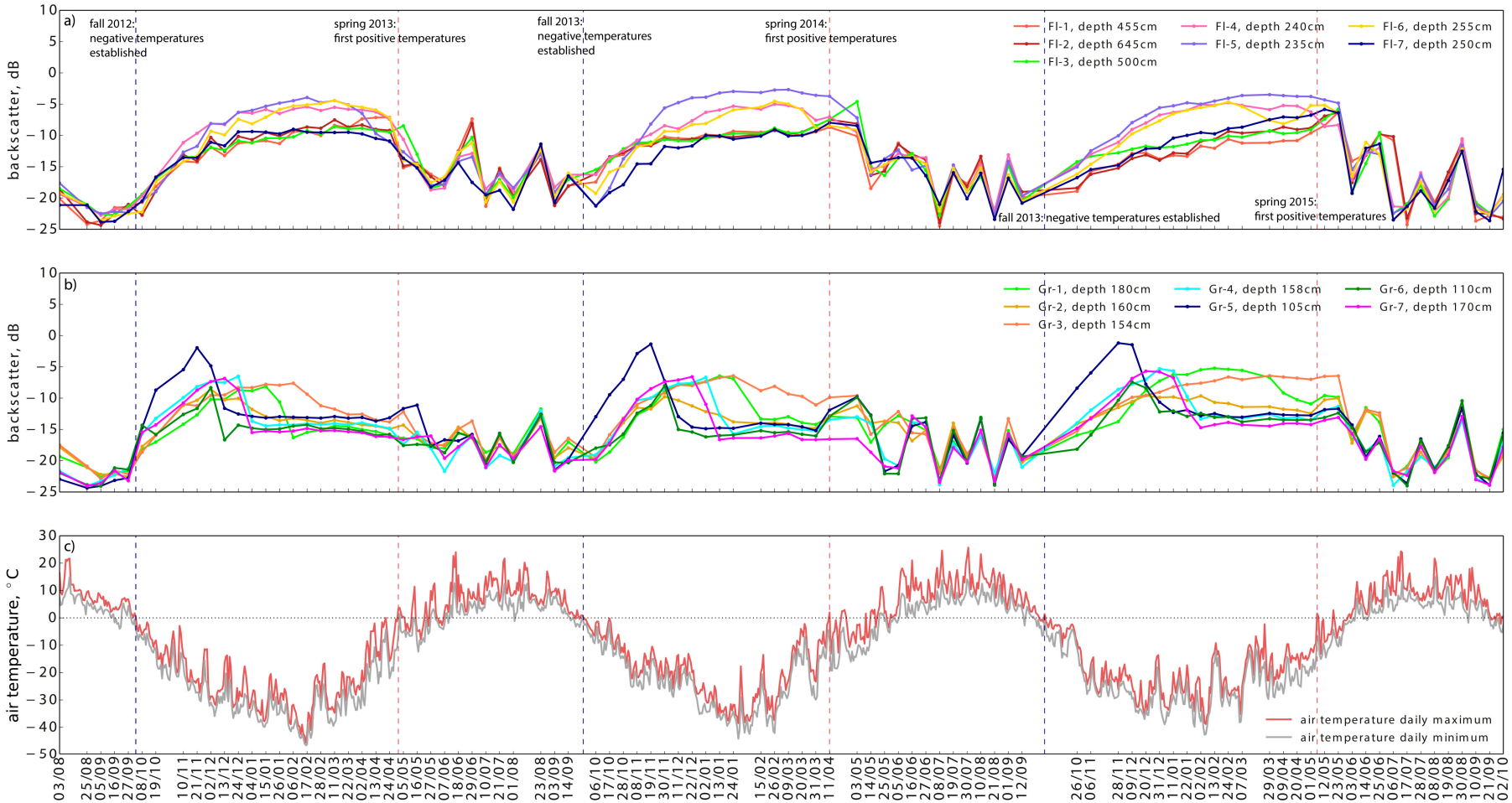

Figure 2. (**a**) TSX backscatter intensity time series for seven deep locations (Fl-1–Fl-7) with presumably floating ice in winter; (**b**) TSX backscatter intensity time series for seven shallow locations (Gr-1–Gr-7) with presumably grounded ice in winter; (**c**) Daily minimum and maximum air temperatures during study period. Dates on x-axis are TSX acquisitions (dd/mm).

5.1. Ice Grounding

5.1.1. Backscatter Intensity Time Series

Based on the in situ measurements obtained in April 2015, we separated seven locations where the ice was floating from seven other locations where the ice was grounded. Backscatter intensity (or simply backscatter) time series for the locations with floating and grounded ice are shown in Figure 2a,b, respectively. The backscatter temporal signatures largely confirmed the separation between the two types of lake ice. Backscatter from the floating ice increased after the freeze onset, then continued to increase gradually and then remained stable over the entire winter (stable stage) until melt onset. Backscatter from the grounded ice featured an abrupt decrease after the ice reached the lake bottom and remained low until surface melt onset. The time of the ice grounding was partly correlated to a location depth: backscatter from the shallowest locations (Gr-5 and Gr-6) decreased earlier than backscatter from deeper locations for all three seasons. Other locations, however, did not fully follow this temporal pattern. Backscatter from two locations (Gr-2 and Gr-3) lacked an abrupt drop but decreased gradually. The decrease in backscatter from Gr-2 lasted for two months in both 2012–2013 and 2013–2014 and resulted in a total decrease of 5.3 dB and 4 dB, respectively. In winter 2014–2015, a slight but consistent decrease in backscatter (2.9 dB in total) from Gr-2 lasted for three months. Backscatter from Gr-3 decreased by 6.2 dB and 5.4 dB in total over periods of three and two months in 2012–2013 and 2013–2014, respectively, but no decrease was demonstrated in 2014–2015. In addition, backscatter from Gr-1 featured a less pronounced drop in 2014–2015 (compared to the two previous years) and decreased gradually over a two month period by 5.2 dB in total. Other locations featured a clear drop in backscatter in the range of 4–13 dB, which lasted 11, 22 or 33 days. For cases when the backscatter drop lasted 22 or 33 days, we defined the time of ice grounding as the first acquisition date of the observed backscatter drop which was greater than the radiometric uncertainty (~1 dB). Table 3 shows the dates of the first backscatter drop and corresponding magnitude of this drop.

Table 3. Timing of the first drop in TSX backscatter intensity for three winter seasons and corresponding values of this drop. Locations are ordered from the deepest to the shallowest.

Location	2012–2013		2013–2014		2014–2015	
	Date of the First Backscatter Drop	Magnitude of the Drop, dB	Date of the First Backscatter Drop	Magnitude of the Drop, dB	Date of the First Backscatter Drop	Magnitude of the Drop, dB
Gr-1, 180 cm	26 January	2.5	15 February *	6.4	9 April	2.5
Gr-7, 170 cm	24 December	1.8	2 January	4.4	22 January	5.2
Gr-2, 160 cm	13 December	1.7	no clear drop		no clear drop	
Gr-4, 158 cm	4 January	7.2	13 January	6	22 January	4.1
Gr-3, 154 cm	17 February	1.8	15 February *	2.4	no drop	
Gr-6, 110 cm	13 December	8.3	11 December	7	31 December	3.8
Gr-5, 105 cm	2 December	2.9	30 November	5.9	20 December	6.3

* No TSX acquisition between 24 January and 15 February 2014: backscatter drop is indicated for 22-day period.

5.1.2. SAR- and CLIMo-Derived Ice Thicknesses Versus in Situ Measured Ice Thicknesses

We used CLIMo to simulate ice thickness for three seasons (Figure 3). Two curves represent two extreme snow cover scenarios, 0% and 100% of snow cover. In situ ice thicknesses of the floating ice locations in April 2015 showed consistency with the simulated ones within the range between 25 and 125%–150% of the snow cover scenarios (for clarity, scenarios other than 0% and 100% are not shown in Figure 3).

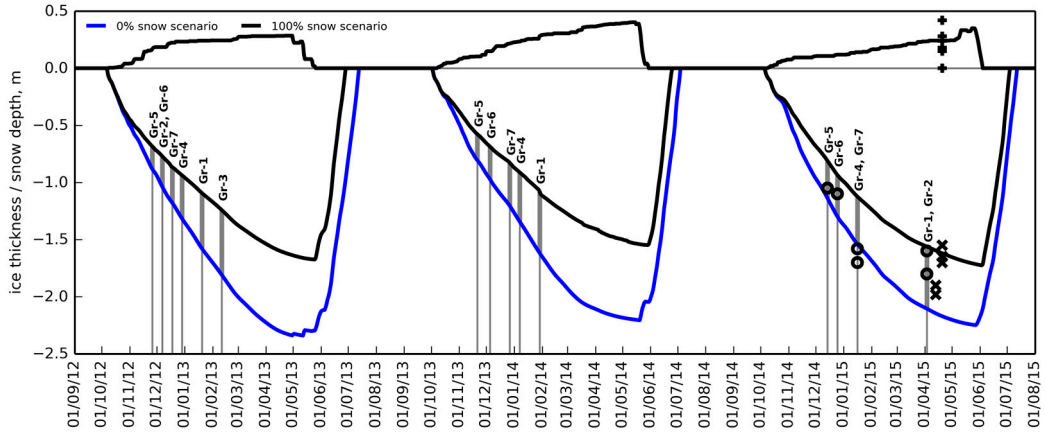

Figure 3. Model simulations of snow on ice and ice thickness for 0% and 100% snow cover scenarios for three ice seasons (2012–2013, 2013–2014, 2014–2015). In situ measured ice thicknesses for the floating locations (Fl-1–Fl-7) are shown with the "×" symbols. In situ measured snow depths are shown with the "+"symbols. Vertical lines correspond to the dates of ice grounding extracted from TSX time series. In situ ice thicknesses (measured in April 2015 at the grounded ice locations) by the time of ice grounding are shown with "o" symbols. Date format on x-axis is dd/mm/yy.

We assigned the time of the first TSX backscatter intensity decrease (i.e., mid-date of the 11-day period) of the seven grounded locations to the simulated ice thickness on those dates. We then compared the simulated ice thicknesses against ice thicknesses measured in situ at grounded locations in April 2015 (Table 4, Figure 3). In situ ice thicknesses were mostly in range of simulated ones in observations in April 2015 reported no snow at the locations Gr-4, Gr-5, Gr-6 and Gr-7 and the presence of snow on ice at locations Gr-1 and Gr-2. Although these snow conditions do not necessarily mean that they were the case for the entire winter, in situ ice thicknesses at lake locations without snow were closer to simulated ones with 0% snow cover scenario, and in situ ice thicknesses at locations with the presence of snow fell between 50% and 75%–100% of snow cover scenarios.

In winters 2012–2013 and 2013–2014, most of the locations showed substantial differences between simulated ice thicknesses and those measured in situ in April 2015, with in situ ice thicknesses typically larger (up to 0.5 m) than that simulated for the two winters, even with a 0% snow cover scenario.

Table 4. Comparison of simulated and in situ measured ice thicknesses by the time of ice grounding.

Location	In Situ Measured Ice Thickness, m (April, 2015)	Simulated Ice Thickness by the Time of Ice Grounding, m (100% to 0% snow cover scenario)		
		2012–2013	2013–2014	2014–2015
Gr-5	1.05	0.68–0.88	0.58–0.81	0.81–1.14
Gr-6	1.1	0.77–1.04	0.69–0.97	0.93–1.3
Gr-3	1.54	1.24–1.81		
Gr-4	1.58	0.94–1.32	0.91–1.34	1.12–1.54
Gr-2	1.6	0.77–1.04		1.56–2.1
Gr-7	1.7	0.86–1.18	0.83–1.2	1.12–1.54
Gr-1	1.8	1.09–1.58	1.08–1.62	1.56–2.1

5.1.3. Spatio-Temporal Variability of Bedfast Ice

Figure 4 shows different selected stages of lake ice development on approximately the same dates (end of November, middle of January, end of March and middle-end of April) of all three seasons for one of the lakes. Spatially, ice grounding began mainly from the northeast- and south oriented shores, whereas other lake margins appeared to be deeper as ice grounding started much later (or did not at all). There was an evident interannual variability in this spatial pattern: by the same time of year,

grounded ice occupied much more area of the lake in the first year than in the second year, while the third year featured dramatically less grounded ice than the previous years.

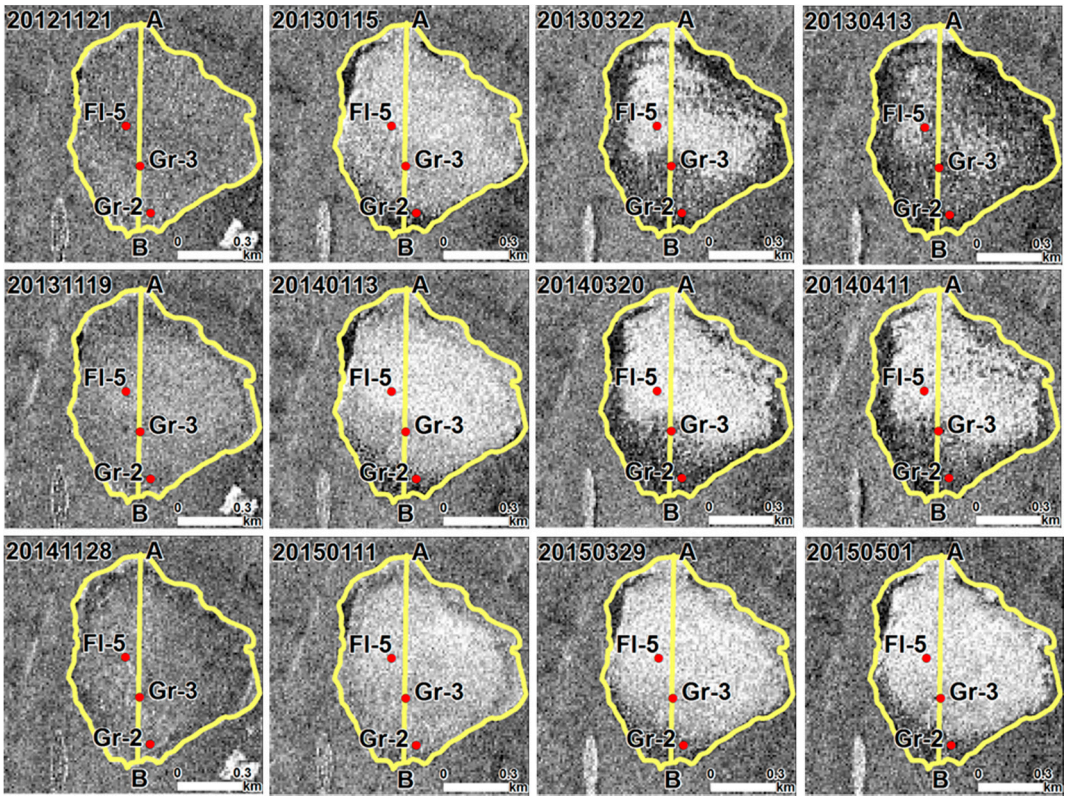

Figure 4. Selected stages of lake ice evolution for ice seasons 2012–2013 (**upper row**), 2013–2014 (**middle row**) and 2014–2015 (**lower row**). Profile A–B is used to represent the spatio-temporal development of backscatter intensity (Figure 5). Date format is yyyymmdd.

In order to demonstrate the spatio-temporal pattern without excluding any of 95 TSX images, we selected a profile across the same lake and produced a time series of backscatter intensity along this profile (Figure 5). The time series shows the progression of ice grounding as darker pixels appear along profile A–B. The ice grounding propagation from the south shore (B) towards the middle of the lake is evident during each of three years, as well as interannual variability reflected in a much smaller area of dark pixels in the last winter compared to the two previous years.

5.1.4. Coherence Time Series

Figure 6 illustrates the difference between grounded and floating ice as revealed on both TSX backscatter intensity and coherence images. Grounded ice appeared dark (low backscatter) in a late winter backscatter image (upper row) due to low return caused by absorption of the SAR signal in the lake bottom sediments. Grounded ice appeared bright (high coherence) in a late winter coherence image (lower row) due to the absence of a change in the backscattering interface between two images, comprising a coherence pair.

In general, well pronounced increases in coherence were observed for all grounded locations in the 2012–2013 season, and for most of the grounded locations in the 2014–2015 seasons (Figure 7). The 2013–2014 season did not feature a well pronounced coherence increase for all grounded locations, but rather variable and generally low coherence. Table 5 presents the periods of the first coherence increase and corresponding coherence values for all grounded locations for the three winter seasons.

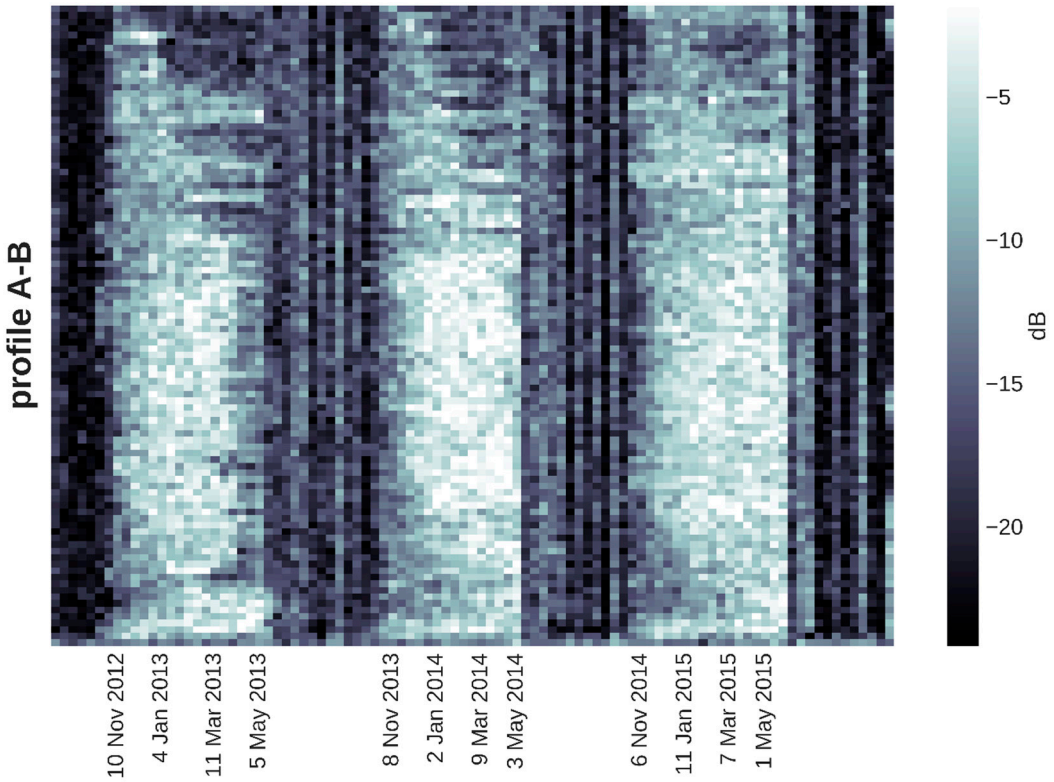

Figure 5. Spatio-temporal evolution of backscatter intensity along profile A–B (from Figure 4).

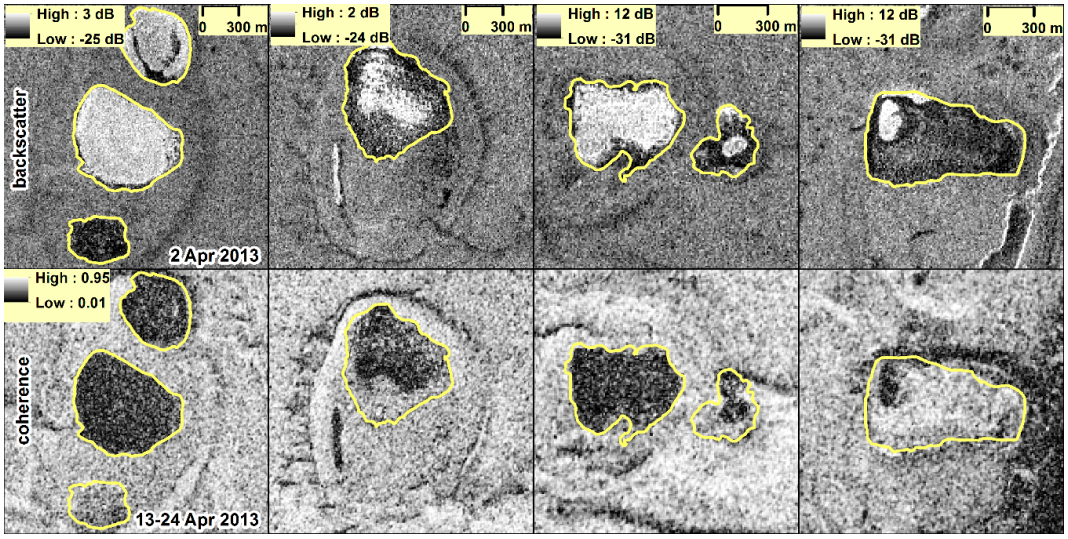

Figure 6. Upper row: late winter backscatter image (2 April 2013) which shows the difference in backscatter for grounded (dark) and floating (bright) ice. **Lower row**: late winter coherence image (13–24 April 2013) which shows the difference in coherence for grounded (bright—higher coherence) and floating (dark—lower coherence) ice.

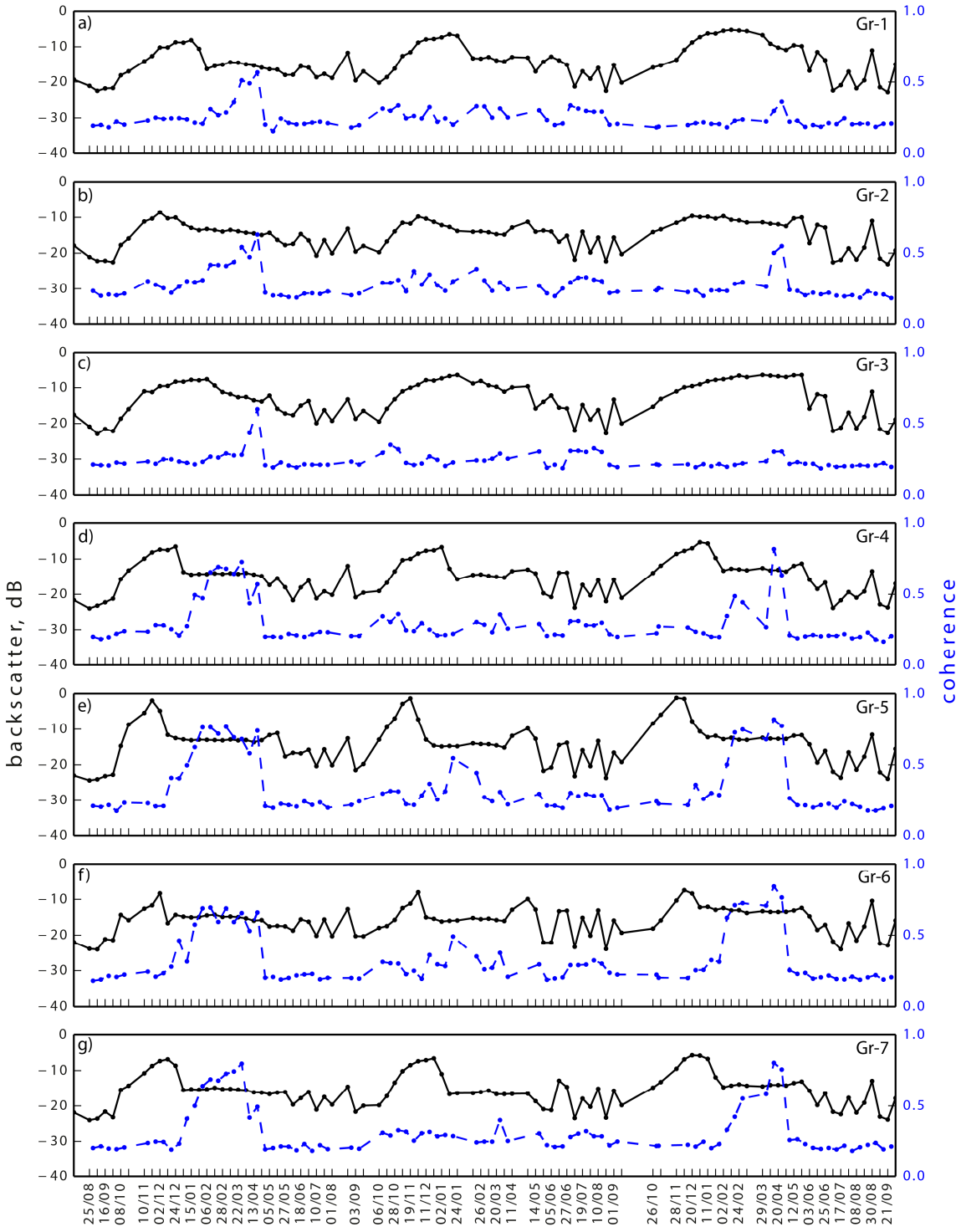

Figure 7. Backscatter intensity (black solid line) and coherence (blue dashed line) time series for all grounded locations over three years (2012–2015): (**a**) Gr-1; (**b**) Gr-2; (**c**) Gr-3; (**d**) Gr-4; (**e**) Gr-5; (**f**) Gr-6; (**g**) Gr-7. Ticks on x-axis are dates of TSX acquisitions (every second tick is labelled). Date format is DD/MM.

Table 5. Periods of the first increase of coherence for three seasons and corresponding coherence values. Locations are ordered from the deepest to the shallowest.

Location	2012–2013		2013–2014		2014–2015	
	Period of the First Coherence Increase	Coherence	Period of the First Coherence Increase	Coherence	Period of the First Coherence Increase	Coherence
Gr-1, 180 cm	6–17 February	0.3	-	-	20 April–1 May	0.36
Gr-7, 170 cm	4–15 January	0.41	20–31 March	0.4	13–24 February	0.42
Gr-2, 160 cm	6–17 February	0.42	-	-	9–20 April	0.5
Gr-4, 158 cm	15–26 January	0.5	-	-	13–24 February	0.49
Gr-3, 154 cm	2–13 April	0.43	-	-	-	-
Gr-6, 110 cm	24 December–4 January	0.46	13–24 January	0.5	2–13 February	0.62
Gr-5, 105 cm	13–24 December	0.4	13–24 January	0.55	2–13 February	0.5

In general, pronounced coherence peaks appeared for the grounded ice locations and the seasons which also featured well pronounced backscatter drops (except for the season 2013–2014 when coherence increase did not occur in most cases). There were some exceptions: location Gr-2 did not demonstrate a well pronounced backscatter drop in the 2014–2015 season, but coherence featured a clear increase for this season (Figure 7b). For most cases, the first increase in coherence occurred later than the first drop of backscatter. The maximum coherence values were observed before spring melt, which was characterized by an abrupt drop in coherence down to values of ~0.2 for all the grounded ice locations.

5.2. Ice Phenology

5.2.1. Freeze Up and Ice Growth

In the fall of 2012, air temperatures fell below 0 °C between the TSX acquisitions of 27 September and 8 October (Figure 2c). The mean backscatter for all locations on 27 September was -22 ± 0.6 dB. On 8 October, the mean backscatter was -20.8 ± 1.1 dB for the deep locations and -16.4 ± 1.6 dB for the shallow locations. Thus, shallow locations showed a clear increase in backscatter between these dates (3.5–8 dB). Detection of the initial freeze-up for the deep locations was hampered by the low contrast between young thin ice cover and calm open water. Shallow locations likely developed a thicker ice cover during this 11-day period than deeper locations, which led to a pronounced backscatter increase for shallow locations. Visual inspection of the image from 8 October revealed that deeper lakes featured bright cracks or ridges whereas the surrounding ice surface appeared dark (Figure 8b), indicating the early stage of freeze-up. After 8 October backscatter began to increase gradually for all lakes. Backscatter from the floating ice locations reached the stable stage around 24 December 2012. The mean backscatter values over the period from 24 December 2012 to 2 April 2013 for the floating ice locations ranged from -9.9 to -5.2 dB (standard deviations between 0.4 and 1.3 dB).

In the fall of 2013, air temperatures fell below 0 °C between 14 September and 6 October TSX acquisitions, but after 25 September (there was no TSX acquisition on 25 September) (Figure 2c). The image of 14 September was slightly affected by wind (Figure 8e), so the mean backscatter for all locations on this date was relatively high (-17.8 ± 1.5 dB) compared to e.g., the previous acquisition. The mean backscatter value calculated from all locations (except of the shallowest location Gr-5) on 6 October was -18.7 ± 1.8 dB. Thus, detection of the initial freeze-up was hampered by the low contrast between wind-affected open water from the previous image and the thin undeveloped ice cover from the latter image. Visual inspection revealed cracks and ridges on the lakes in the image of 6 October, indicative of the presence of ice (Figure 8f). After 6 October, backscatter began to increase gradually for all locations. Backscatter from the floating ice locations reached the stable stage around 30 November 2013. The mean backscatter values over the period from 30 November 2013 to 11 April 2014 for the floating ice locations ranged from -10.2 to -3.6 dB (standard deviations between 0.5 dB and 1.7 dB).

In the fall of 2014, air temperatures fell below 0 °C between 12 September and 26 October of the TSX acquisitions (there were no TSX acquisitions on 23 September as well as on 4 and 15 October) (Figure 2c). The three missing images did not allow us to detect the initiation of freeze-up. However, the mean backscatter intensity for all locations (except of the shallowest location Gr-5) increased during this period from -20 ± 0.6 dB to -15.9 ± 1.6 dB. The mean backscatter values over the period from 31 December 2014 to 1 May 2015 for the floating ice locations ranged from -11.7 to -4.3 dB (standard deviations between 0.6 dB and 1.8 dB).

At the stable stage, deeper floating locations (Fl-1, Fl-2 and Fl-3) showed lower backscatter intensity (by ~4 dB) than shallower floating locations (Fl-4, Fl-5 and Fl-6) for all three winter seasons, with the exception of the rather shallow location Fl-7 featuring lower backscatter in the order of backscatter values from deeper locations (Table 6, Figure 2a).

Table 6. Mean backscatter intensity for the floating ice locations during the stable stage for three seasons.

Location	Depth, m	Ice Thickness, m	Mean Backscatter in 2012–2013 (24 December–2 April), dB	Mean Backscatter in 2013–2014 (30 November–11 April), dB	Mean Backscatter in 2014–2015 (31 December–1 May), dB
Fl-1	4.55	1.9	-9.8 ± 1.3	-9.7 ± 0.5	-11.7 ± 1.2
Fl-2	6.45	1.98	-9.2 ± 1	-9.7 ± 1	-10.5 ± 1.8
Fl-3	5.0	1.55	-9.9 ± 0.9	-9.7 ± 1	-10.4 ± 1
Fl-4	2.4	1.65	-6 ± 0.4	-6.6 ± 1.3	-5.6 ± 0.6
Fl-5	2.35	1.65	-5.2 ± 0.8	-3.6 ± 0.8	-4.3 ± 0.7
Fl-6	2.55	1.65	-5.9 ± 1.2	-7.2 ± 1.7	-6.3 ± 1.2
Fl-7	2.5	1.7	-9.5 ± 0.2	-10.2 ± 1.1	-8.9 ± 1.6

5.2.2. Melt Onset

Melt onset marks the beginning of snow or ice surface melt during the break-up period. In spring 2013, a decrease in backscatter in the range of 2.7–8.1 dB was observed for deep locations between 24 April and 5 May (with the exception of Fl-5 showing a 3.2 dB decrease between 2 and 13 April and Fl-3 showing 4.5 dB decrease between 5 and 16 May) (Figure 2a). Shallow locations did not demonstrate a clear pattern (Figure 2b): the time when backscatter intensity began to deviate from its stable stage varied from 5 May to 7 June for different locations, and deviations were both negative and positive. Intermittent positive air temperatures were first detected between 24 April and 5 May 2013 (Figure 2c). A strong coherence drop occurred between 24 April and 5 May (Figure 7).

In spring 2014, a prominent backscatter decrease in the range of 5.9–10.4 dB occurred between 3 and 14 May for deep locations (Figure 2a). For shallow locations, the same period corresponded to a more moderate backscatter decrease of 1.1–3.9 dB (Figure 2b). Backscatter intensity alterations already began between 31 March and 11 April for some shallow locations. Intermittent positive air temperatures were first detected between 31 March and 11 April (Figure 2c).

In spring 2015, a significant backscatter decrease in the range of 7.8–13.2 dB occurred between 23 May and 3 June for deep locations (Figure 2a). For shallow locations, the same time period corresponded to a backscatter decrease in the range of 2.4–9.4 dB (Figure 2b). Positive air temperatures were reached during this time period as well (Figure 2c). However, some shallow locations revealed a slight increase in backscatter (up to 2.2 dB) between 1 and 12 May. A strong coherence drop occurred between 1 and 12 May (Figure 7).

5.2.3. Water-Clear-of-Ice

Water-clear-of-ice corresponds to the date when a water body becomes completely ice-free (i.e., it marks the end of the break-up period). In the summer of 2013, water-clear-of-ice was detected on 10 July for all lakes (Figure 8d), while most of the lakes were covered by ice on the image of 29 June (previous acquisition) (Figure 8c).

In summer 2014, water-clear-of-ice was detected on 8 July for all lakes (Figure 8h). The previous image (27 June, Figure 8g) was affected by wind (wind speed at 08:30 local time was 5.7 m/s).

However, comparing this image with the image of 29 June 2013 (Figure 8c), acquired under similar wind conditions (wind speed of 5.2 m/s), partial ice coverage was apparent on the latter image. Thus, the lakes were likely already ice free on 27 June 2014.

In the summer of 2015, water-clear-of-ice was detected on 17 July (Figure 8l), while the image from 6 July featured significant ice cover presence on some lakes (Figure 8k).

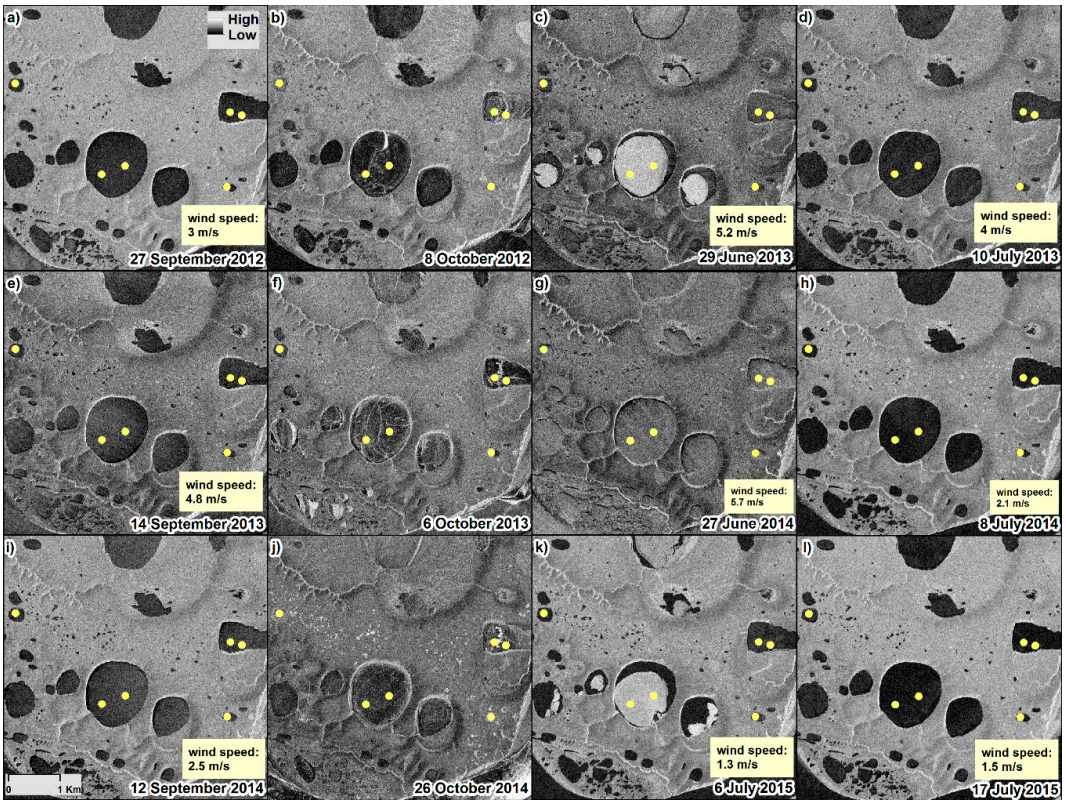

Figure 8. Sub-areas of TSX intensity maps showing events in the ice phenology cycle for three ice seasons: (**a**–**d**) 2012–2013; (**e**–**h**) 2013–2014; (**i**–**l**) 2014–2015. Yellow dots are drilling locations. Wind speed measurements are from automatic weather station on Kurungnakh Island at 08:30 local time of TSX acquisition day (TSX acquisition is at 08:34 local time).

6. Discussion

6.1. Ice Grounding

6.1.1. Backscatter Intensity

Our results demonstrate that TSX backscatter intensity is a viable tool for the monitoring of floating/grounded lake ice regimes. Backscatter intensity signatures mostly confirmed the in situ measurements from April 2015: locations where the ice was found grounded showed a drop in backscatter, whereas floating ice locations exhibited a stable backscatter over the entire winter. Out of 21 cases (seven grounded locations and three years), 14 showed a very well pronounced backscatter drop, and seven exhibited a smooth backscatter decrease over a few months without a distinct drop. We relate the lack of such a manifest in backscatter drop to be associated with the selection of the ROIs (group of pixels) which might include a mixed signal from both floating and grounded ice. The choice of the ROIs was based on drilling locations where the ice thickness was measured in situ. These locations were georeferenced using a simple handheld Garmin GPS device, which has an accuracy of about 10 m. Therefore, to ensure that the ROI includes the drilling point, the size of ROI was chosen to be about 100 m in diameter. Consequently, the lake ice thickness could vary

spatially within the ROI with ice being partly grounded or floating. Such non-uniform ice grounding can also be naturally caused by heterogeneous lake bathymetry, especially when a ROI is chosen during a transition between the shallow littoral zone and the deeper pelagic zone. This issue has also been raised by Brown et al. [39] in the detection of fish overwintering pools under the ice on the Sagavanirktok River, Alaska, using ASAR C-band with 30 m spatial resolution. In particular, they found that backscatter intensity was influenced by both presence of floating and grounded ice at the edge of the pools surveyed in the field.

On the one hand, the TSX time series with its 11-day temporal resolution improves the accuracy of the extraction of the timing of ice grounding, compared to previous studies using RADARSAT (with 24-day repeat cycle) or ERS (35 days) data. On the other hand, the multistep drop in backscatter intensity for a number of cases in our study poses difficulties for precise identification of the timing of ice grounding. We assume that the first decrease of backscatter larger than the radiometric uncertainty of TSX (~1 dB) indicates ice grounding. One possible reason for a subsequent backscatter decrease, if present, can be the freezing of sediments. Morris et al. [25] found that ERS-1 backscatter intensity from grounded lake ice was about 3 dB higher for a sub-Arctic site compared to an Arctic site. They hypothesized that the lake sediments might not have been completely frozen but still rather wet at the warmer sub-Arctic site, which could explain why the radar return was higher for this site. This assumption may also apply to our case, but rather in a temporal than a spatial context: after the first backscatter decrease lake sediments were potentially wet and not completely frozen, and the following freezing of sediments caused the backscatter to decrease further. A better understanding of SAR signal response to freezing of lake sediments can help towards more confident extraction of the timing of ice grounding in the future. Another possible explanation for the multistep backscatter decrease is non-uniform grounding of the ice: some zones of the ice bottom within the ROI (or even within resolution cell) could be already attached to the bottom whereas other zones were still not grounded, causing backscatter to continue to decrease. By the time the ice became completely bedfast, backscatter intensity stabilized. The same situation could also be considered at the microscale where ice crystals attach to the lake bottom non-uniformly, leaving some pockets with liquid water. A combination of all of the above described processes could also possibly take place.

Various applications could be developed or improved based on explored TSX data. Detection of the lakes with bedfast ice could be useful for the estimation of fish habitat areas and water availability in winter. Fraction of bedfast ice could be estimated on different scales for the assessment of taliks distribution in permafrost. Transition between the bedfast and floating ice regime of a lake could be used as a proxy for the interannual variations in water level or maximum ice thickness.

6.1.2. Model Results

For the first time, Jeffries et al. [26] used ERS-1-derived timing of ice grounding together with the model CLIMo to retrieve the maximum depth of shallow lakes on the Alaskan North Slope; however, no validation of the results was made. Kozlenko and Jeffries [32] used the same approach, data and study area to map the bathymetry of shallow lakes and used existing bathymetric maps for the validation, which showed only moderate agreement. We used the same approach and retrieved ice thicknesses at the grounded locations using TSX time series and the model CLIMo. Among the improvements of our study are the better temporal resolution of the SAR time series (11 days compared to 35 days of ERS) and the in situ measured thicknesses of grounded ice. Comparison of retrieved and in situ ice thicknesses showed a reasonably good agreement in the 2014–2015 season, and a divergence in the previous two years, with in situ ice thicknesses typically larger than simulated. Assuming that the timing of ice grounding was derived correctly, this suggests that the water level could have been higher in fall 2014 prior to ice formation than in previous years, leading to thicker ice in winter of 2014–2015.

6.1.3. Spatio-Temporal Variability of Bedfast Ice

The present work mainly focuses on the temporal evolution of TSX parameters for a number of discrete locations where in situ ice thickness measurements were available. However, the spatio-temporal evolution of ice grounding for an entire lake is of high importance, for instance, for the extraction of the bathymetry or for interannual monitoring. Our results show a great potential of TSX imagery with its high spatial and temporal resolution to track the progression of ice grounding on a lake (see also video in Supplementary Materials). All three years demonstrated different fractions of grounded ice by the end of the winter, with a maximum in 2012–2013 and a minimum in 2014–2015. Since simulations with CLIMo revealed similar maximum ice thicknesses in 2012–2013 (2.34 m for 0 snow cover and 1.67 m for 100% snow cover) and 2014–2015 (2.25 m for 0% snow cover and 1.73 m for 100% snow cover), we assume that variations in water levels could result in such significant differences in the grounded ice patterns between the two years.

6.1.4. Coherence

The increase of coherence at grounded locations served as an additional indicator of ice grounding. This increase often occurred later than the drop in backscatter by 2–5 TSX repeat cycles, which can possibly be explained by the following: when the freezing front reaches the depth when all the sediments are dry (water content of sediments likely decreases with depth), the backscatter becomes stable. The coherence is defined by both amplitude and phase components of the signal and is therefore more sensitive to changes in the backscattering interface. Therefore, the coherence can stay low when the freezing front propagates into the wet sediments. We hypothesize that the first increase of coherence can indicate the stage when the wet layer of sediments becomes frozen and dry, and the maximal coherence can indicate the complete freezing of the sediments before melt onset. Therefore, coherence time series appear to be less robust compared to backscatter intensity time series for estimation of the timing of ice grounding. However, an increase of coherence can help with the detection of ice grounding when the backscatter does not show a clear signal, as for instance in the case of location Gr-2 during winter 2014–2015. Additionally, the coherence time series appears to have the potential for monitoring the freezing of the lake sediments.

Generally low and rather variable (compared to other winters) coherence was observed during the winter of 2013–2014. Such low coherence does not necessarily indicate the absence of lake ice grounding, but can be related to environmental factors on the lake ice surface such as changing snow conditions due to snowfall and snow drifting [53].

The high coherence observed for the shallow lakes in the ice seasons 2012–2013 and 2014–2015 should theoretically allow performing an interferometric analysis and generate maps of lake bathymetry, which will be the focus of future work.

6.2. Ice Phenology

6.2.1. Freeze Onset

Our results demonstrate that TSX backscatter intensity time series can generally be used to monitor lake ice phenology. The freeze-up was characterized by a gradual increase in backscatter, but the very initial stage of ice formation (-21 to -19 dB) was often indiscernible from a calm open water surface. This was also reported in previous studies [24,27]. Cracks and ridges featured high backscatter intensities compared to the surrounding dark young ice cover, supporting the detection of freeze-up, as reported in previous studies [17]. A few missing images (which were not acquired by TSX due to reasons unknown to us) exactly during freeze-up periods of fall 2013 and 2014 prevented us from discerning the time of freeze onset with confidence (at least not in the order of 11 days) and from comparing freeze onset on an interannual basis. However, simulations with CLIMo did provide an independent and useful complementary estimate of ice-on dates for the deep and shallow lakes when TSX images were not available every 11 days (Table 7).

The mature stage of ice development for the floating locations was characterized by stable backscatter intensity in the range of −12 to −3.5 dB, which is well within the range of previous investigations [20,27]. Floating ice locations mostly exhibited interannual consistency of backscatter values at the stable stage: every location yielded a similar mean backscatter from year to year, which indicates relatively constant ice growth conditions for each location.

Table 7. Dates of ice-on and ice-off derived from TSX images and simulated with CLIMo.

	Ice-on TSX (Deep and Shallow)	Ice-on CLIMo (Deep)	Ice-on CLIMo (Shallow)	Ice-off TSX	Ice-off CLIMo
2012–2013	Between 27 September and 8 October	7 October	3 October	Latest by 10 July (29 June shows significant ice coverage)	30 June–15 July (depending on snow cover scenario)
2013–2014	Between 14 September and 6 October (one missing image in between)	4 October	27 September	By 27 June (based on comparison with previous year because image is affected by wind)	26 June–6 July (depending on snow cover scenario)
2014–2015	Three missing images	7 October	27 September	Latest by 17 July (6 July shows significant ice coverage for some big lakes)	6 July–14 July (depending on snow cover scenario)

6.2.2. Melt Onset

Melt onset was detected in most cases by a prominent backscatter decrease (up to 13 dB) from its stable stage; however, some cases also showed an increase in backscatter. Such contrasting backscatter changes have previously been reported by Jeffries et al. and Morris et al. [24,25] (C-band) for snow covered lake ice and by Strozzi et al. [54] for terrestrial snow cover (C-band and Ka-band). A decrease in backscatter can be explained by the wetting of snow or ice surface leading to a reduced signal penetration, while backscatter increase can be observed in the case of the formation of ice crusts caused by melt and refreeze cycles.

In the present study, melt onset was well detected by a significant coherence drop in the 2012–2013 and 2014–2015 winter seasons, consistent in time for all grounded locations. Snow melt causes a coherence loss due to a complete change in the nature of the backscattering target [55,56]. Therefore, such a consistent coherence drop is potentially a better indicator of melt onset, since backscatter intensity exhibited a variability in the timing of its deviations from the stable stage, and, moreover, deviations were both positive and negative. It is also possible that the prominent backscatter intensity drop was rather caused by water ponding on the snow or ice surface than by snow melt. Antonova et al. [56] showed a minor backscatter increase (max. 3 dB) over terrestrial landscape units for the same TSX dataset for the snow melt period of 2013 and related this increase to the rough crust formation on the snow surface due to melt and refreeze cycles. Since backscatter for deep locations over the same time period showed a significant drop (3–8 dB), we hypothesize that this drop was caused by water ponding on the ice surface and expand this hypothesis to the following years as well. Some studies indicated that meltwater ponding does not affect floating ice as much as grounded ice due to water percolation through the ice column and lateral water drainage off the floating ice [57]. Nonetheless, it is reasonable to assume that the observed backscatter drops in our study are too large to be only related to snow melt. In the ice season 2012–2013, the assumed water ponding on the lakes surface coincided with a strong coherence drop (24 April–5 May). In the ice season 2013–2014, a drop in coherence was not observed due to generally low coherence over the entire winter season. In 2014–2015, a strong drop in coherence occurred earlier (1–12 May) than the strong backscatter drop associated with possible water ponding (23 May–3 June). Although coherence appears to be more robust for the detection of melt onset than TSX backscatter, its use is limited to the shallow lakes characterized by bedfast ice.

6.2.3. Water-Clear-of-Ice

Water-clear-of-ice was mainly detected by visual inspection of the backscatter intensity images, which featured open water with low backscatter. Estimated ice-off dates with TSX are within the range of those obtained with CLIMo (Table 7). In 2013–2014, ice-off was about two weeks earlier than in 2012–2013, and in 2014–2015 ice-off was about one week later than in 2012–2013 (note the uncertainty in the order of 11 days due to TSX revisit cycle). The ice season 2013–2014 featured the thinnest CLIMo simulated ice of all three seasons which could partly explain the earliest ice-off date in this year.

The temporal resolution of TSX (11 days) is rather coarse for the ice phenology monitoring [27]. However, for remote Arctic sites where in situ observations are very sparse and rare, and optical imagery is strongly affected by clouds and limited daylight, the TSX revisit cycle can still be useful. Using TSX images from different orbits can significantly improve temporal coverage, but this complicates the method as one must take into account different acquisition geometries. SAR data from recently launched Sentinel-1 satellites with their revisit cycle of 6 days can significantly improve temporal resolution for the repeat-pass SAR monitoring of lake ice phenology.

7. Conclusions

The main goal of this study was to examine the potential of a unique X-band SAR dataset to monitor ice phenology and bedfast ice on a number of thermokarst lakes in the Siberian Arctic. Three-year repeat-pass TSX time series with high temporal (11 days) and spatial (10 m) resolution were used. Two different parameters derived from SAR imagery were employed in the analysis: backscatter intensity and 11-day interferometric coherence. In addition, the evolution of ice thickness and dates of ice-on and ice-off were simulated using the lake ice model CLIMo. Ground-truthing based on field measurements of ice thickness was available from 14 locations during the late winter (13–20 April) of the last year of time series. The following conclusions can be drawn from this study:

- Ice phenology stages, such as (i) the onset of freezing as well as ice thickening; (ii) the onset of surface melt; and (iii) the date of complete ice-off condition were generally tracked by TSX backscatter intensity time series. Dates of ice-on and ice-off were in range of those simulated by CLIMo. The onset of the surface melt was marked by a strong drop in coherence, which was more time-consistent for different locations than changes in backscatter intensity.
- Lake ice grounding was well detected by a prominent drop in TSX backscatter intensity in winter. Most of the field measurements confirmed the TSX-derived separation between floating and bedfast ice. An increase in interferometric coherence was observed for grounded ice for two of the three ice seasons, confirming the detection of bedfast ice. The gradual increase of coherence occurred typically later than the backscatter drop, probably reflecting the freezing of lake sediments.
- The high temporal resolution of the TSX time series (compared to previous satellite-based SAR studies) generally improved the extraction of the timing of ice grounding. However, we encountered some difficulties in the timing extraction, which are likely related to (i) a mixed signal from both floating and grounded ice within the ROI and (ii) propagation of the freezing front into lake sediments which affects SAR signal return.
- Using the timing of ice grounding and simulated ice thickness we obtained the water depth at grounded ice locations where in situ ice thicknesses were available. Comparison showed a reasonably good agreement in the year of field measurements and a larger difference in the previous two years.
- Both ice phenology and ice grounding revealed interannual variability, most likely due to a difference in climatic conditions and water levels between the years.
- The high spatial and temporal resolution of TSX imagery allows monitoring the progression of the ice grounding for an entire lake which could be used for lake bathymetry extraction in future. Furthermore, the high coherence observed over the shallow lakes indicates that the bathymetry of these lakes could be derived with SAR interferometry in future studies.

Supplementary Materials: The following are available online at www.mdpi.com/2072-4292/8/11/903/s1, Video S1: TSX backscatter intensity time series showing the evolution of bedfast ice on the lake from Figure 4. Video S2: TSX backscatter intensity time series showing the evolution of bedfast ice on one of the studied lakes. Video S3: TSX backscatter intensity time series showing the evolution of bedfast ice on one of the studied lakes.

Acknowledgments: We thank anonymous reviewers for their valuable comments which helped to improve the manuscript. We thank the German Aerospace Center DLR and Achim Roth for invaluable help with the data access. We also thank Homa Kheyrollah Pour for the running CLIMo, Grant Gunn for valuable discussions and Sina Muster for the critical reading of the manuscript. We are grateful for the assistance in the field from Niko Bornemann and the support of the research station "Samoylov Island". This research has been conducted partly with the support of the Helmholtz Alliance HA310 'Remote Sensing and Earth System Dynamics' and partly with DAAD (German Academic Exchange Service) scholarship (Kurzstipendien für Doktoranden 2015/16 (57044996)) to S. Antonova. This research was also supported by a Discovery Grant from the Natural Sciences and Engineering Council of Canada (NSERC) to C. Duguay. A. Kääb acknowledges support by the European Research Council under the European Union's Seventh Framework Programme (FP/2007–2013)/ERC grant agreement No. 320816, and A. Kääb and S. Westermann by the ESA DUE GlobPermafrost project (4000116196/15/IN-B).

Author Contributions: The article is a result of collaboration with all listed co-authors. S. Westermann encouraged the idea of the study; C. Duguay and S. Antonova designed and conducted the study; S. Antonova analyzed the data and wrote the paper; A. Kääb, B. Heim, M. Langer and J. Boike contributed valuable advice and comments.

Conflicts of Interest: The authors declare no conflict of interests.

References

1. Lafleur, P.M.; Wurtele, A.B.; Duguay, C.R. Spatial and temporal variations in surface albedo of a subarctic landscape using surface-based measurements and remote sensing. *Arct. Alp. Res.* **1997**, *29*, 261–269. [CrossRef]
2. Pienitz, R.; Doran, P.T.; Lamoureux, S.F. Origin and geomorphology of lakes in the polar regions. In *Polar Lakes and Rivers: Limnology of Arctic and Antarctic Aquatic Ecosystems*; Warwick, F.V., Laybourn-Parry, J., Eds.; Oxford University Press: Oxford, UK, 2008; pp. 25–41.
3. Grosse, G.; Jones, B.; Arp, C. Thermokarst lakes, drainage, and drained basins. In *Treatise on Geomorphology*; Shroder, J.F., Giardino, R., Harbor, J., Eds.; Academic Press: San Diego, CA, USA, 2013; Volume 8, pp. 325–353.
4. Zimov, S.A.; Voropaev, Y.V.; Semiletov, I.P.; Davidov, S.P.; Prosiannikov, S.F.; Chapin, F.S., III; Trumbore, S.; Tyler, S. North Siberian lakes: A methane source fueled by Pleistocene carbon. *Science* **1997**, *277*, 800–802. [CrossRef]
5. Rouse, W.R.; Oswald, C.J.; Binyamin, J.; Spence, C.; Schertzer, W.M.; Blanken, P.D.; Bussières, N.; Duguay, C.R. Role of northern lakes in a regional energy balance. *J. Hydrometeorol.* **2005**, *6*, 291–305. [CrossRef]
6. Brown, L.C.; Duguay, C.R. The response and role of ice cover in lake-climate interactions. *Prog. Phys. Geogr.* **2010**, *34*, 671–704. [CrossRef]
7. Langer, M.; Westermann, S.; Muster, S.; Piel, K.; Boike, J. The surface energy balance of a polygonal tundra site in northern Siberia Part 2: Winter. *Cryosphere* **2011**, *5*, 509–524. [CrossRef]
8. Lenormand, F.; Duguay, C.R.; Gauthier, R. Development of a historical database for the study of climate change in Canada. *Hydrol. Process.* **2002**, *16*, 3707–3722. [CrossRef]
9. Duguay, C.R.; Prowse, T.D.; Bonsal, B.R.; Brown, R.D.; Lacroix, M.P.; Ménard, P. Recent trends in Canadian lake ice cover. *Hydrol. Process.* **2006**, *20*, 781–801. [CrossRef]
10. Jeffries, M.O.; Zhang, T.; Frey, K.; Kozlenko, N. Estimating late-winter heat flow to the atmosphere from the lake dominated Alaskan North Slope. *J. Glaciol.* **1999**, *45*, 315–324. [CrossRef]
11. Langer, M.; Westermann, S.; Walter Anthony, K.; Wischnewski, K.; Boike, J. Frozen ponds: Production and storage of methane during the Arctic winter in a lowland tundra landscape in northern Siberia, Lena River delta. *Biogeosciences* **2015**, *12*, 977–990. [CrossRef]
12. Arp, C.D.; Jones, B.M.; Lu, Z.; Whitman, M.S. Shifting balance of thermokarst lake ice regimes across the Arctic Coastal Plain of northern Alaska. *Geophys. Res. Lett.* **2012**, *39*, L16503. [CrossRef]
13. Surdu, C.M.; Duguay, C.R.; Brown, L.C.; Fernández Prieto, D. Response of ice cover on shallow lakes of the North Slope of Alaska to contemporary climate conditions (1950–2011): Radar remote-sensing and numerical modeling data analysis. *Cryosphere* **2014**, *8*, 167–180. [CrossRef]
14. Arp, C.D.; Jones, B.M.; Urban, F.E.; Grosse, G. Hydrogeomorphic processes of thermokarst lakes with grounded-ice and floating-ice regimes on the Arctic coastal plain, Alaska. *Hydrol. Process.* **2011**, *25*, 2422–2438. [CrossRef]

15. Latifovic, R.; Pouliot, D. Analysis of climate change impacts on lake ice phenology in Canada using the historical satellite data record. *Remote Sens. Environ.* **2007**, *106*, 492–507. [CrossRef]
16. Weber, H.; Riffler, M.; Nõges, T.; Wunderle, S. Lake ice phenology from AVHRR data for European lakes: An automated two-step extraction method. *Remote Sens. Environ.* **2016**, *174*, 329–340. [CrossRef]
17. Hall, D.K.; Fagre, D.B.; Klasner, F.; Linebaugh, G.; Liston, G.E. Analysis of ERS-1 synthetic aperture radar data of frozen lakes in northern Montana and implications for climate studies. *J. Geophys. Res. Oceans* **1994**, 22473–22482. [CrossRef]
18. Howell, S.E.L.; Brown, L.C.; Kang, K.-K.; Duguay, C.R. Variability in ice phenology on Great Bear Lake and Great Slave Lake, Northwest Territories, Canada, from SeaWinds/QuikSCAT: 2000–2006. *Remote Sens. Environ.* **2009**, *113*, 816–834. [CrossRef]
19. Cook, T.L.; Bradley, R.S. An analysis of past and future changes in the ice cover of two High-Arctic lakes based on synthetic aperture radar (SAR) and Landsat imagery. *Arct. Antarct. Alp. Res.* **2010**, *42*, 9–18. [CrossRef]
20. Surdu, C.M.; Duguay, C.R.; Kheyrollah Pour, H.; Brown, L.C. Ice freeze-up and break-up detection of shallow lakes in Northern Alaska with spaceborne SAR. *Remote Sens.* **2015**, *7*, 6133–6159. [CrossRef]
21. Elachi, C.; Bryan, M.L.; Weeks, W.F. Imaging radar observations of frozen Arctic lakes. *Remote Sens. Environ.* **1976**, *5*, 169–175. [CrossRef]
22. Weeks, W.F.; Sellmann, P.; Campbell, W.J. Interesting features of radar imagery of ice-covered North Slope lakes. *J. Glaciol.* **1977**, *18*, 129–136.
23. Weeks, W.F.; Fountain, A.G.; Bryan, M.L.; Elachi, C. Differences in radar return from ice-covered North Slope Lakes. *J. Geophys. Res. Oceans* **1978**, *83*, 4069–4073. [CrossRef]
24. Jeffries, M.O.; Morris, K.; Weeks, W.F.; Wakabayashi, H. Structural-stratigraphic features and ERS-1 SAR backscatter characteristics of ice growing on shallow lakes in NW Alaska, winter 1991–92. *J. Geophys. Res. Oceans* **1994**, *99*, 22459–22471. [CrossRef]
25. Morris, K.; Jeffries, M.O.; Weeks, W.F. Ice processes and growth history on Arctic and sub-Arctic lakes using ERS-1 SAR data. *Polar Rec.* **1995**, *31*, 115–128. [CrossRef]
26. Jeffries, M.O.; Morris, K.; Liston, G.E. A method to determine lake depth and water availability on the North Slope of Alaska with spaceborne imaging radar and numerical ice growth modelling. *Arctic* **1996**, *49*, 367–374. [CrossRef]
27. Duguay, C.R.; Pultz, T.J.; Lafleur, P.M.; Drai, D. RADARSAT backscatter characteristics of ice growing on shallow sub-Arctic lakes, Churchill, Manitoba, Canada. *Hydrol. Process.* **2002**, *16*, 1631–1644. [CrossRef]
28. Duguay, C.R.; Lafleur, P.M. Determining depth and ice thickness of shallow sub-Arctic lakes using space-borne optical and SAR data. *Int. J. Remote Sens.* **2003**, *24*, 475–489. [CrossRef]
29. Hirose, T.; Kapfer, M.; Bennett, J.; Cott, P.; Manson, G.; Solomon, S. Bottomfast ice mapping and the measurement of ice thickness on tundra lakes using C-Band Synthetic Aperture Radar remote sensing. *J. Am. Water Resour. Assoc.* **2008**, *44*, 285–292. [CrossRef]
30. Jones, B.M.; Gusmeroli, A.; Arp, C.D.; Strozzi, T.; Grosse, G.; Gaglioti, B.V.; Whitman, M.S. Classification of freshwater ice conditions on the Alaskan Arctic Coastal Plain using ground penetrating radar and TerraSAR-X satellite data. *Int. J. Remote Sens.* **2013**, *34*, 8253–8265. [CrossRef]
31. Sobiech, J.; Dierking, W. Observing lake- and river-ice decay with SAR: advantages and limitations of the unsupervised k-means classification approach. *Ann. Glaciol.* **2013**, *54*, 65–72. [CrossRef]
32. Kozlenko, N.; Jeffries, M.O. Bathymetric mapping of shallow water in thaw lakes on the North Slope of Alaska with spaceborne imaging radar. *Arctic* **2000**, *53*, 306–316. [CrossRef]
33. Gunn, G.E.; Duguay, C.R.; Brown, L.C.; King, J.; Atwood, D.; Kasurak, A. Freshwater lake ice thickness derived using X- and Ku-band FMCW scatterometers. *Cold Reg. Sci. Technol.* **2015**, *120*, 115–126. [CrossRef]
34. Kaatze, U.; Uhlendorf, V. The dielectric properties of water at microwave frequencies. *Zeitschrift für Physikalische Chemie* **1981**, *126*, 151–165. [CrossRef]
35. Vant, M.R.; Gray, R.B.; Ramseier, R.O.; Makios, V. Dielectric properties of fresh and sea ice at 10 and 35 GHz. *J. Appl. Phys.* **1974**, *45*, 4712–4717. [CrossRef]
36. Engram, M.; Walter Anthony, K.M.; Meyer, F.J.; Grosse, G. Characterization of L-band synthetic aperture radar (SAR) backscatter from floating and grounded thermokarst lake ice in Arctic Alaska. *Cryosphere* **2013**, *7*, 1741–1752. [CrossRef]

37. Atwood, D.K.; Gunn, G.E.; Roussi, C.; Wu, J.; Duguay, C.; Sarabandi, K. Microwave backscatter from Arctic lake ice and polarimetric implications. *IEEE Trans. Geosci. Remote Sens.* **2015**, *53*, 5972–5982. [CrossRef]
38. Hoekstra, P.; Delaney, A. Dielectric properties of soils at UHF and microwave frequencies. *J. Geophys. Res.* **1974**, *79*, 1699–1708. [CrossRef]
39. Brown, R.S.; Duguay, C.R.; Mueller, R.P.; Moulton, L.L.; Doucette, P.J.; Tagestad, J.D. Use of Synthetic Aperture Radar (SAR) to identify and characterize overwintering areas of fish in ice-covered arctic rivers: A demonstration with Broad Whitefish and their habitats in the Sagavanirktok River, Alaska. *Trans. Am. Fish. Soc.* **2010**, *139*, 1711–1722. [CrossRef]
40. Gunn, G.E.; Brogioni, M.; Duguay, C.; Macelloni, G.; Kasurak, A.; King, J. Observation and modeling of X-and Ku-band backscatter of snow-covered freshwater lake ice. *IEEE J. Sel. Top. Appl. Earth Obs. Remote Sens.* **2015**, *8*, 3629–3642. [CrossRef]
41. Zebker, H.A.; Villasenor, J. Decorrelation in interferometric radar echoes. *IEEE Trans. Geosci. Remote Sens.* **1992**, *30*, 950–959. [CrossRef]
42. Geldsetzer, T.; van der Sanden, J.; Brisco, B. Monitoring lake ice during spring melt using RADARSAT-2 SAR. *Can. J. Remote Sens.* **2010**, *36*, S391–S400. [CrossRef]
43. Grigoriev, N.F. The temperature of permafrost in the Lena Delta basin: Deposit conditions and properties of the permafrost in Yakutia (in Russian). *Yakutsk* **1960**, *2*, 97–101.
44. Muster, S.; Langer, M.; Heim, B.; Westermann, S.; Boike, J. Subpixel heterogeneity of ice-wedge polygonal tundra: a multi-scale analysis of land cover and evapotranspiration in the Lena River Delta, Siberia. *Tellus B* **2012**, *64*, 17301. [CrossRef]
45. Boike, J.; Kattenstroth, B.; Abramova, K.; Bornemann, N.; Chetverova, A.; Fedorova, I.; Fröb, K.; Grigoriev, M.; Grüber, M.; Kutzbach, L.; et al. Baseline characteristics of climate, permafrost and land cover from a new permafrost observatory in the Lena River Delta, Siberia (1998–2011). *Biogeosciences* **2013**, *10*, 2105–2128. [CrossRef]
46. Morgenstern, A.; Grosse, G.; Günther, F.; Fedorova, I.; Schirrmeister, L. Spatial analyses of thermokarst lakes and basins in Yedoma landscapes of the Lena Delta. *Cryosphere* **2011**, *5*, 849–867. [CrossRef]
47. Werner, C.; Wegmüller, U.; Strozzi, T.; Wiesmann, A. Gamma SAR and interferometric processing software. In Proceedings of the ERS-Envisat Symposium, Gothenburg, Sweden, 16–20 October 2000.
48. Duguay, C.R.; Flato, G.M.; Jeffries, M.O.; Ménard, P.; Morris, K.; Rouse, W.R. Ice-cover variability on shallow lakes at high latitudes: model simulations and observations. *Hydrol. Process.* **2003**, *17*, 3465–3483. [CrossRef]
49. Jeffries, M.O.; Morris, K.; Duguay, C.R. Lake ice growth and decay in central Alaska, USA: Observations and computer simulations compared. *Ann. Glaciol.* **2005**, *40*, 195–199. [CrossRef]
50. Brown, L.C.; Duguay, C.R. A comparison of simulated and measured lake ice thickness using a Shallow Water Ice Profiler. *Hydrol. Process.* **2011**, *25*, 2932–2941. [CrossRef]
51. Reliable Prognosis RP5. Available online: http://rp5.ru/Weather_archive_on_Stolb_Island (accessed on 18 October 2016).
52. Sturm, M.; Liston, G.E. The snow cover on lakes of the Arctic Coastal Plain of Alaska, USA. *J. Glaciol.* **2003**, *49*, 370–380. [CrossRef]
53. Rott, H.; Nagler, T.; Scheiber, R. Snow mass retrieval by means of SAR interferometry. In Proceedings of the FRINGE Workshop (ESA SP-550), Frascati, Italy, 1–5 December 2003.
54. Strozzi, T.; Wiesmann, A.; Mätzler, C. Active microwave signatures of snow covers at 5.3 and 35 GHz. *Radio Sci.* **1997**, *32*, 479–495. [CrossRef]
55. Strozzi, T.; Wegmuller, U.; Matzler, C. Mapping wet snowcovers with SAR interferometry. *Int. J. Remote Sens.* **1999**, *20*, 2395–2403. [CrossRef]
56. Antonova, S.; Kääb, A.; Heim, B.; Langer, M.; Boike, J. Spatio-temporal variability of X-band radar backscatter and coherence over the Lena River Delta, Siberia. *Remote Sens. Environ.* **2016**, *182*, 169–191. [CrossRef]
57. Arp, C.D.; Jones, B.M.; Liljedahl, A.K.; Hinkel, K.M.; Welker, J.A. Depth, ice thickness, and ice-out timing cause divergent hydrologic responses among Arctic lakes. *Water Resour. Res.* **2015**, *51*, 9379–9401. [CrossRef]